

Supporting Information

Self-Powered Composites by Bioinspired Device-to-Material Integration

Guojiang Wen, Zhiwei Zhu, Wenrui Cai, Zhongfeng Ji, Hua Li, Chengye Ma, Ziyu Zhao, Shanshan Lv, Jiarui Yang, Xuewei Fu, Wei Yang and Yu Wang**

College of Polymer Science and Engineering, State Key Laboratory of Polymer Materials Engineering, Sichuan University, Chengdu, 610065, Sichuan, China

Corresponding authors:

Xuewei Fu (xuewei.fu@scu.edu.cn); ORCID: 0000-0002-1164-427X

Yu Wang (yu.wang3@scu.edu.cn); ORCID: 0000-0003-1155-9144

1. Experimental Section

1.1 Materials

CR927 and CR1220 coin cells with different sizes were purchased from Putian New Bonneville Company Limited. The cathode primarily consisted of MnO₂ and the anode primarily consisted of lithium alloy. Glass fiber was used as the separator. The electrolyte consisted of dimethoxymethane, propylene carbonate, and lithium perchlorate. The standard white resin for 3D printing was provided by Shenzhen Anycubic Technology Company Limited, with a curing wavelength of 405 nm, bending strength of 40-60 MPa, and bending modulus of 600-750 MPa. Silicon rubber (Ecoflex 00-30) was provided from Smooth-On, with the elongation at a break of 400 % - 600 %. Monofilament nickel (Ni) wires (Ni ≥ 99.99 %) with different diameters of 100, 150, and 200 μm were supplied from Jiangsu Zhonghang Metal Company Limited. Conductive copper adhesive tape and silver conductive paste were purchased from Guangdong Canrd New Energy Technology Company Limited. Thermoplastic polyurethane (TPU, Elastollan 1185A FHF) was purchased from Badische Anilin-und-Soda-Fabrik (BASF) Company Limited. N, N-Dimethylformamide (DMF) was purchased from Tianjin Bodi Chemical Company Limited. Ethanol (purity > 99.7%) was obtained from Shanghai Fine Chemical Reagent Company Limited. All materials and reagents were obtained from commercial suppliers and used directly without any purification process unless otherwise explained.

1.2 Preparation of self-powered composites (SPCs)

In brief, 2 g of TPU particles were dissolved in 8 g DMF solvent and stirred in the 60 °C water bath for 2 hours to obtain a homogeneous solution. Subsequently, the solution was subjected to ultrasonic treatment for 2 hours to eliminate bubbles. A stainless steel scraper with a 200 μm gap was used to cast a layer of TPU solution onto

a glass plate, which was placed in a 60 °C air oven for 2 hours to form a uniformly thick elastic film. Subsequently, the TPU film was cut into 3 mm × 90 mm rectangles. Conductive copper tape (3 mm × 16 mm) was then affixed to the surface of the TPU film at 10 mm intervals to make interdigitated conductive strips. A 3D solid model was designed using Rhinoceros software (Robert McNeel, USA) to accommodate coin cells with different layouts. The 3D model was exported in STL format and subsequently imported into the printer. The digital slicing process was employed to segment the model into a sequence of 2D layers, which were utilized to control the UV projection for curing the acrylic resin within the vat. The resin mold for housing the coin cells was processed using the Photon Mono (M5s, Anycubic, China) UV-curing 3D printer. This printer produced three-dimensional structures by crosslinking the acrylic resin layer-by-layer in the specified areas using ultraviolet light. The printer head was lifted and lowered repeatedly, with each layer cured at the bottom of the vat, until the entire three-dimensional object was fully formed. The layer thickness and exposure time were set to 50 μm and 3.5 seconds, respectively. Upon completion of the printing, the finished model was ultrasonically washed with ethanol and further UV-cured for 10 minutes. Subsequently, the CR927 coin cells were inserted into the mold, and the conductive path was established by connecting the TPU conductive film. Conductive silver paste was applied to the interface between the film and the coin cells, following to cure at room temperature for 4 hours to achieve a strong bond. The interface between the male and female molds was bonded and cured using adhesive, creating the SPC with a size of 55 mm × 25 mm × 12 mm. Additionally, a cylindrical support mold featuring a central groove was fabricated using identical 3D printing parameters, designed to accommodate the 90° coin cells with dimensions of 20 mm × 3 mm, for mechanical compression testing purposes.

The mixture of equal proportions of components A and B from Ecoflex 00-30 silicone rubber was thoroughly blended and then subjected to vacuum degassing for 2 minutes. The well-mixed silicone rubber was subsequently injected into a PP

transparent plastic tube with an inner diameter of 3 mm and cured to form a silicone rubber elastomer with a diameter of 3 mm. A stretchable conductor was fabricated employing a multifunctional twisting machine (YH-2018B, China) to uniformly wrap a 0.15 mm nickel metal wire around a 3 mm diameter silicone rubber elastomer (Length of 25 mm). A multifunctional spot welding machine (Z001, Kechen Electronics Co., China) was employed to weld nickel metal lugs onto the upper and lower surfaces of a CR927 coin cell, coated with insulating rubber. To fabricate a unified entity, seven coin cell batteries were serially connected using 25 mm long stretchable conductors, thereby forming the single circuit. Subsequently, Ecoflex 00-30 silicone rubber was cast and cured in grooved mold with curing time of 3 hours and groove dimensions of 175 mm \times 8 mm, to fabricate the flexible SPCs (21.7 V) based on silicone rubber materials.

1.3 Characterizations

The constant velocity impact testing of individual coin cells was conducted using an electronic universal testing machine with a 10 kN load sensor (AGS-X-10kN, Shimadzu Instruments Manufacturing Co., Ltd, China). Coin cells were positioned between two metal plates, with the anode being the upper surface. A loading plate was employed to apply a compressive force to the sample in the direction of the metal plate, and a 20-mm metal insulating cylinder was integrated into the standard upper metal plate as a compression probe, thereby inducing a mechanical load on the sample. The compression rate was set at 1 mm/min. The load and displacement during the compression process were recorded to determine the compression strength of the tested sample. When the specified strain (0 %, 24.7 %, 47.8 %, 60.3 %) was reached, the stress applied by the machine was unloaded. The voltage of the coin cell was immediately measured using a multimeter at the instant of stress release. Subsequently, the voltage of the compressed coin cell battery sample was recorded 5 minutes after relaxation. Electrochemical impedance spectroscopy (EIS) was performed using the Princeton

electrochemical workstation (Princeton-ParStat 400, USA) in the frequency range of 10^6 to 1 Hz with an amplitude of 5 mV at open-circuit voltage after the coin cell had been compressed and left for 2 hours. The discharge capacity and curves of the coin cell under different compression treatments were recorded using the Neware battery testing system at a constant current of 0.1 mA. After mechanical testing, the coin cells were disassembled, and the cathode and separator were harvested for characterization. A high-definition camera (HY-5100, China) was used to capture the appearance and crack distribution of the cathode (after separator removal) with different strains (0 %, 24.7 %, 47.8 %, and 60.3 %). Subsequently, the cathode was ground into powders using a pestle and mortar. The crystal structure of the powdered cathode was analyzed by using powder X-ray diffraction (Ultima IV, Rigaku Co., Ltd, Japan) with 2θ scan range of 5° - 90° . Scanning electron microscopy (SEM, Hitachi Regulus 8220, Japan) was used to analyze the microstructure of the glass fiber separator removed from the coin cells.

Three-point bending properties of SPCs were evaluated using an electronic universal testing machine equipped with a 10 kN load sensor (AGS-X-10kN, Shimadzu Instruments Manufacturing Co., Ltd, China). For each sample, the span between the supports was set at 40 mm, and the compression rate was maintained at 1 mm/min. During the experiment, the load on the sensor and the displacement of the downward-moving metal cylinder were recorded and utilized to calculate the stress and strain of the sample. 5 parallel samples were set up to ensure the reliability and stability of the data results. During the three-point bending process, the voltage measurement system (Keithley 2400 Signal Source Meter, USA) was employed to monitor and record the voltage changes of the sample in real time. The strain experienced by the sample was calculated using Equation (1):

$$\varepsilon = \frac{6sh}{L^2} \quad (1)$$

Where, s represented the downward displacement of the sample, h was the thickness of the sample, and L was the span of the three-point bending fixture.

The stress experienced by the sample was calculated using Equation (2):

$$\sigma = \frac{3FL}{2bh^2} \quad (2)$$

Where, F represented the applied load, h represented the thickness of the sample, L was the span of the three-point bending fixture, and b was the width of the sample.

Stretch-recovery cycling performance of the stretchable conductor was investigated by using the advanced dynamic rheometer (Discovery HR20, TA Instruments, USA) with a stretching rate of 1 mm/min. Two testing protocols were established to assess the stability of the stretchable conductor during use: an ultimate tensile program and multiple cyclic tensile test programs. During the tensile tests, the modified resistivity measurement system (Keithley 2400 source meter, USA) was employed to simultaneously record the changes in the resistance of the stretchable conductor, with a constant current of 0.1 mA applied during the test. The tests were repeated three times to obtain an average value for the final results. The tensile and failure behavior of the flexible stretchable power source based on silicone rubber was measured using an electronic universal testing machine equipped with a 500 N load sensor (AGS-X, SHIMADZU, China). The modified voltage measurement system (Keithley 2400 source meter, USA) was utilized to synchronously record the voltage changes of the flexible stretchable power source during the test. Furthermore, the voltage changes of the flexible stretchable power source were recorded under various deformation modes, including bending, twisting, and knotting, as well as at different stretching rates, such as rapid stretching, slow stretching, and pulsed slow stretching.

1.4 Modeling of stress distribution

The stress distribution of the polymer host without or with five coin cells embedded with different placement angles (0°, 45°, and 90°) was studied. The commercial finite element software package COMSOL Multiphysics was employed to

solve the steady-state solid mechanics equilibrium equations, which were fundamentally expressed in equation (3):

$$\nabla \cdot \boldsymbol{\sigma} + \mathbf{F} = 0 \quad (3)$$

Where, $\boldsymbol{\sigma}$ represented the stress tensor and the \mathbf{F} denoted the body force.

We applied a boundary loading $\boldsymbol{\sigma}_A$ to the model to analyze the stress distribution under fixed loading conditions in our calculation.

$$\mathbf{S} \cdot \mathbf{n} = \boldsymbol{\sigma}_A \quad (4)$$

Here, \mathbf{S} represented the Piola-Kirchhoff stress tensor; \mathbf{n} denoted the boundary normal vector, and $\boldsymbol{\sigma}_A$ was the stress value applied at the boundary.

To mimic the three-point bending test process, we established the following boundary conditions:

$$\mathbf{u}|_{p_i} = 0 \quad (5)$$

Here, p_i contained 8 points of the model.

To enhance the convergence speed of the model, we incrementally increased the value of $\boldsymbol{\sigma}_A$ from 0.01 MPa to 1 MPa.

The material parameters and model parameters used in the calculations are detailed in **Table S1**.

2. Supplementary figures and table

Table S1. Main parameters of the FEM model

Parameters	Value
σ_A , <i>MPa</i>	1
Length of resin box, <i>mm</i>	55
Width of resin box, <i>mm</i>	25
Height of resin box, <i>mm</i>	12
Density of resin box, <i>kg/m³</i>	932
Young's modulus of resin box, GPa	0.4
Poisson's ratio of resin box	0.3
Angle of Inclination	[0°, 45°, 90°]
Thickness of battery case, <i>mm</i>	0.2
The diameter of battery case, <i>mm</i>	9.5
The height of battery case, <i>mm</i>	2.7
Density of battery case, <i>kg/m³</i>	7930
Young's modulus of battery case, GPa	200
Poisson's ratio of battery case	0.3
P_i	[(-25, -12.5,0), (-25,12.5,0), (25,-12.5,0), (25,12.5,0), (-25, -12.5,6), (-25,12.5,6), (25, -12.5,6), (25,12.5,6)]

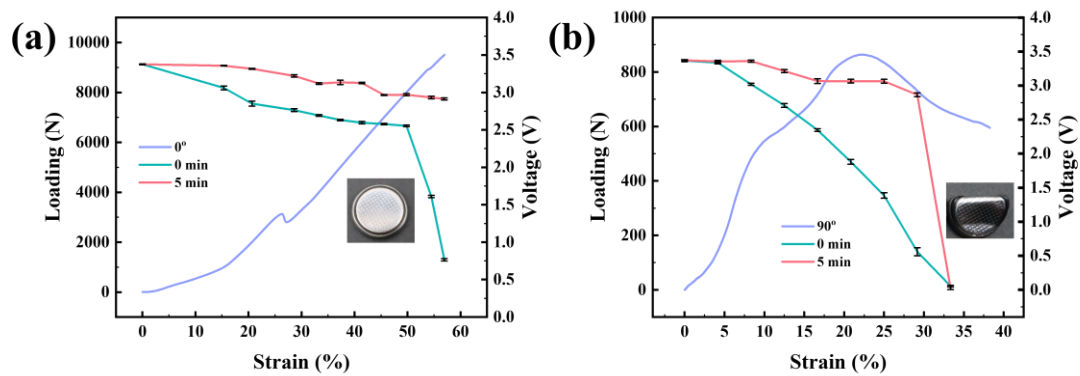


Figure S1. The load-strain and real-time voltage of the CR1220 coin cells subjected to constant-speed impact at 1 mm/min for (a) 0° and (b) 90°.

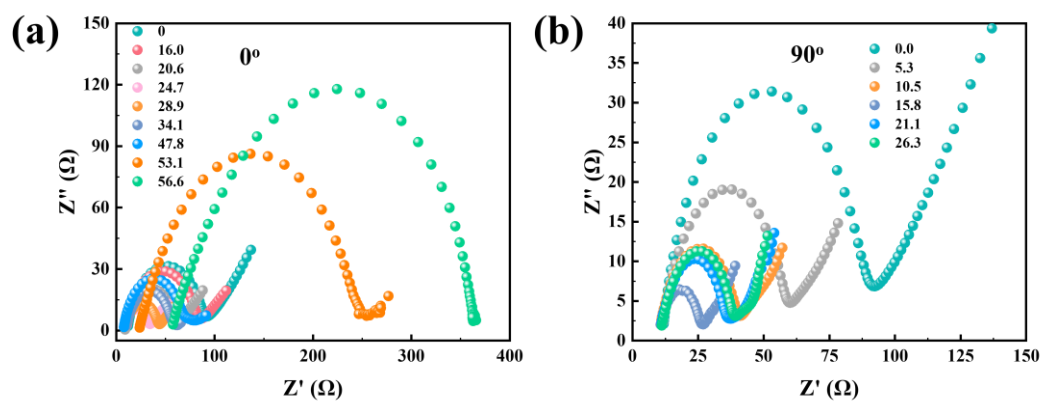


Figure S2. Nyquist plots of CR927 coin cells subjected to constant-speed impact at 1 mm/min for different strain values and placement angle of (a) 0° and (b) 90° .

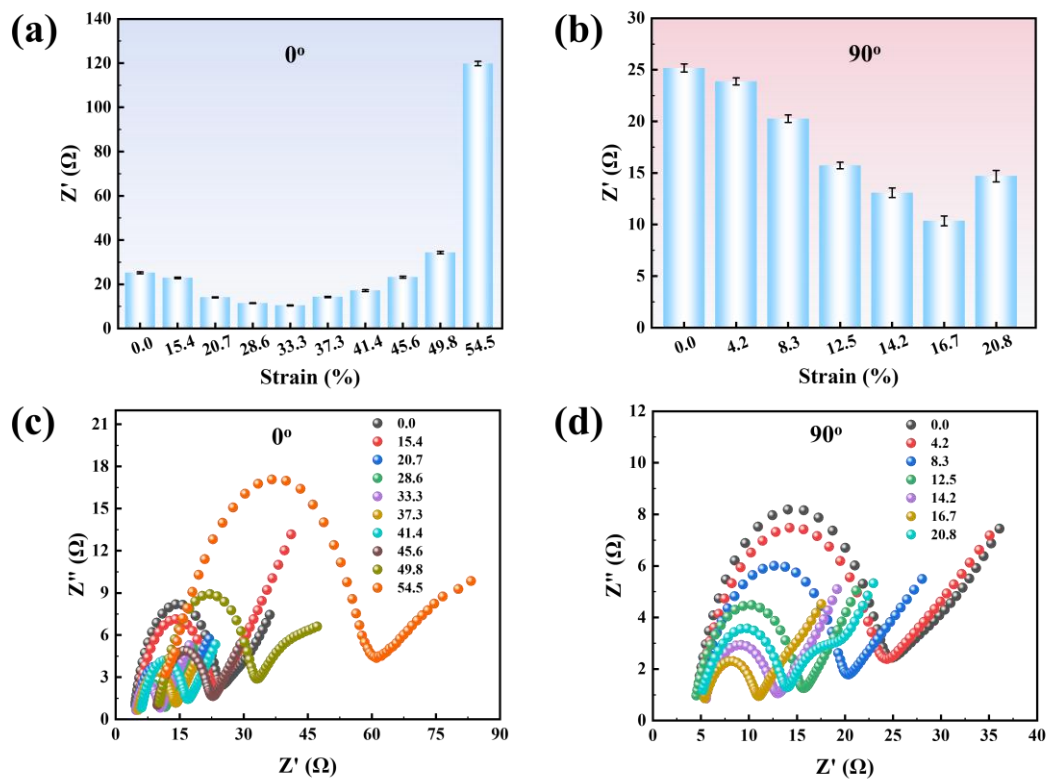


Figure S3. Summary of cell resistance of CR1220 coin cells subjected to constant-speed impact at 1 mm/min with (a) 0° and (b) 90° placement. Nyquist plots of (c) 0° and (d) 90° placement.

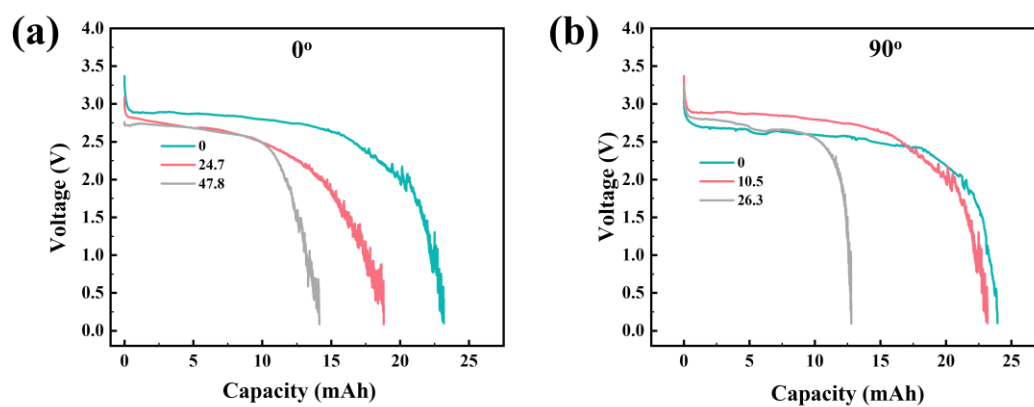


Figure S4. Voltage curves of CR927 coin cells with (a) 0° and (b) 90° placement at a constant impact speed of 1 mm/min with fixed discharge current of 0.1 mA.

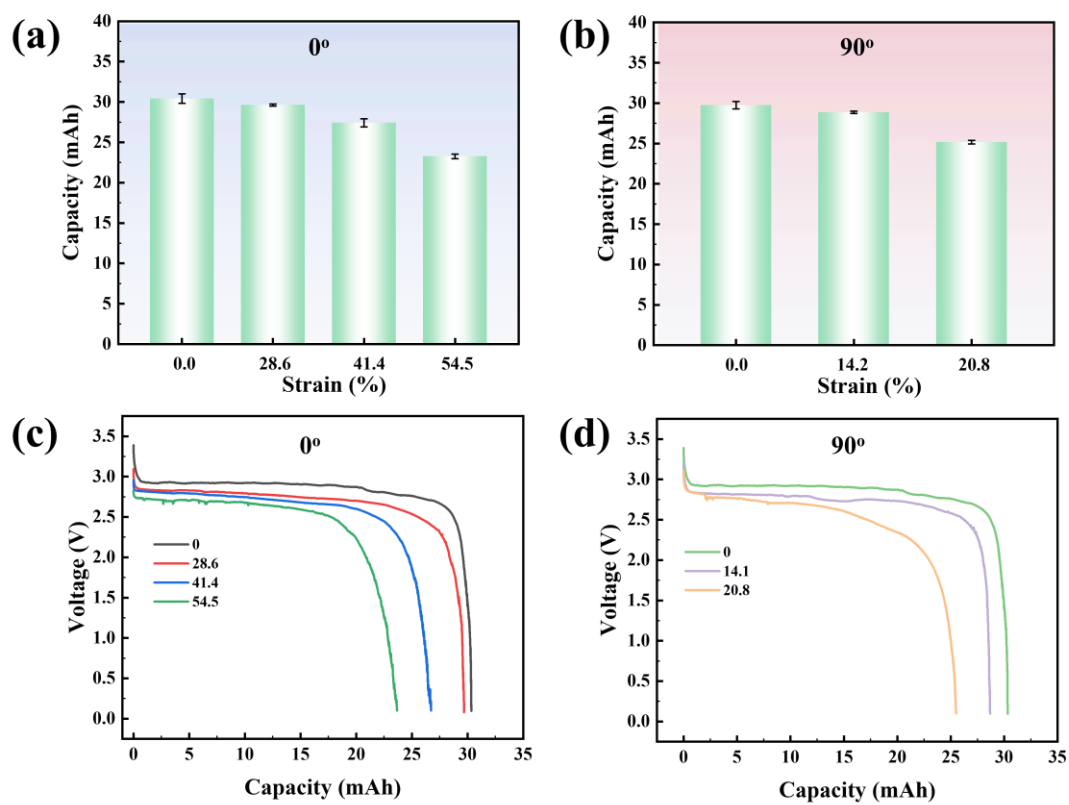


Figure S5. Summary of discharge capacity of CR1220 coin cells subjected to constant-speed impact at 1 mm/min with (a) 0° and (b) 90° placement. Voltage curves for (c) 0° and (d) 90° placement measured at constant discharge current of 0.1 mA.

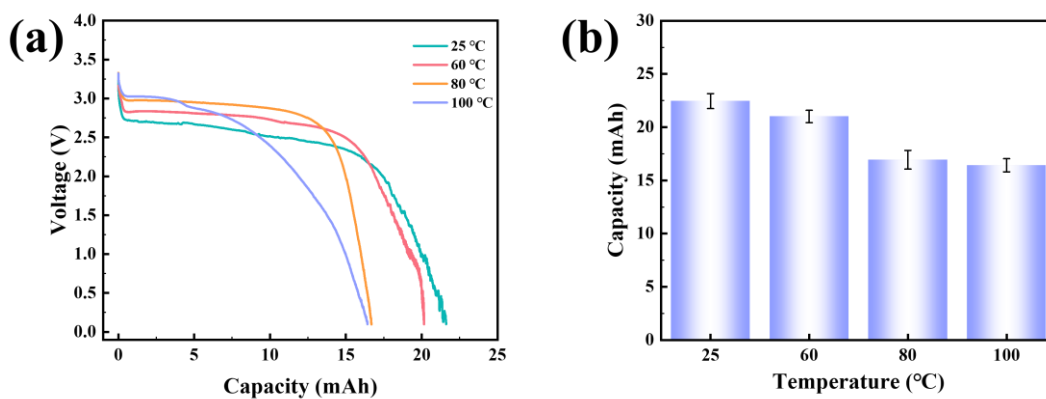


Figure S6. (a) Discharging curves and (b) discharging capacity of CR927 coin cell at different temperatures with a discharging current of 0.1 mA.



Figure S7. Photographs of CR927 coin cells subjected to constant-speed impact of 1 mm/min with 0° placement at different strains.


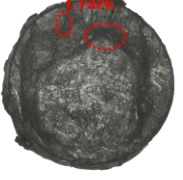


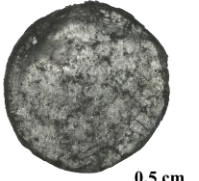
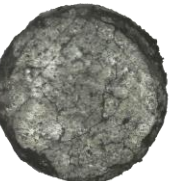

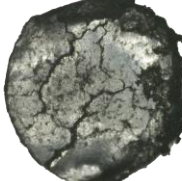
Strain value	0 %	24.7 %	47.8 %	60.3 %
Separator side				
Cathode shell side				

Figure S8. Photographs of the cathodes (0° placement) subjected to compression at constant speed of 1 mm/min with different strains.

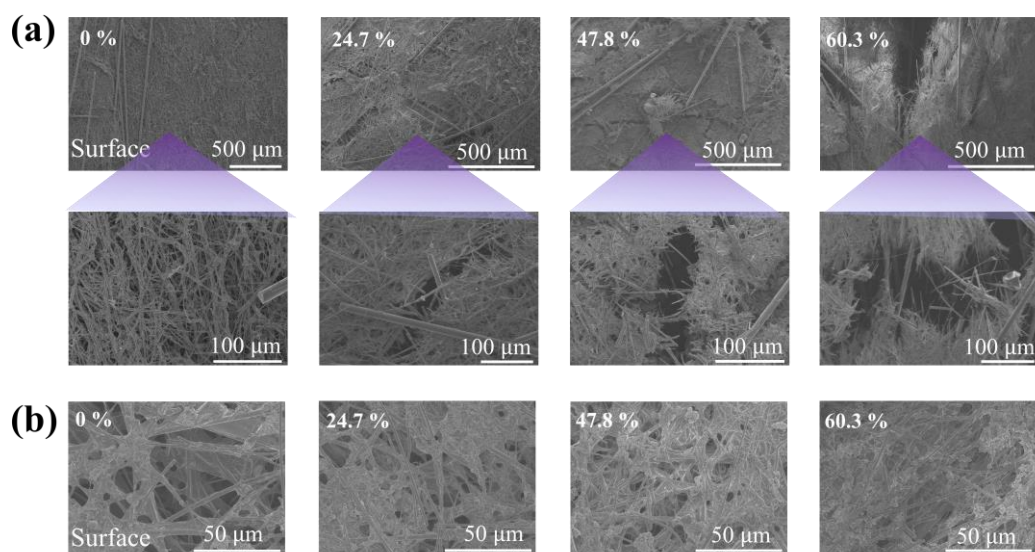


Figure S9. SEM images of separators (0° placement) subjected to compression at constant speed of 1 mm/min with different strains: (a) toward anode side and (b) toward cathode side.

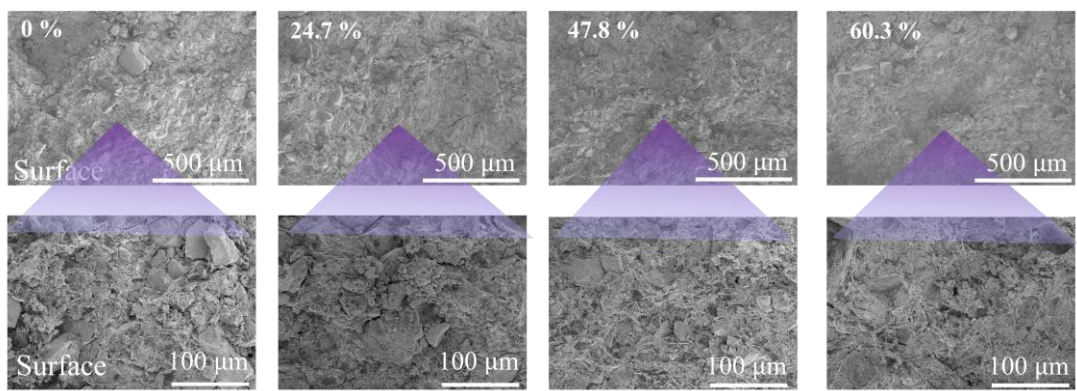


Figure S10. SEM images of cathodes (0° placement) with different strains.

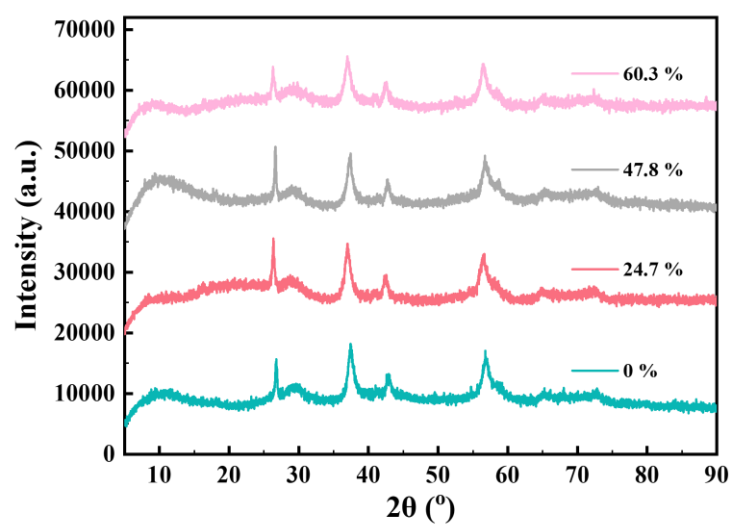


Figure S11. X-ray diffraction patterns of the cathode material (mainly composed of MnO₂) for the CR927 coin cell with different strains.

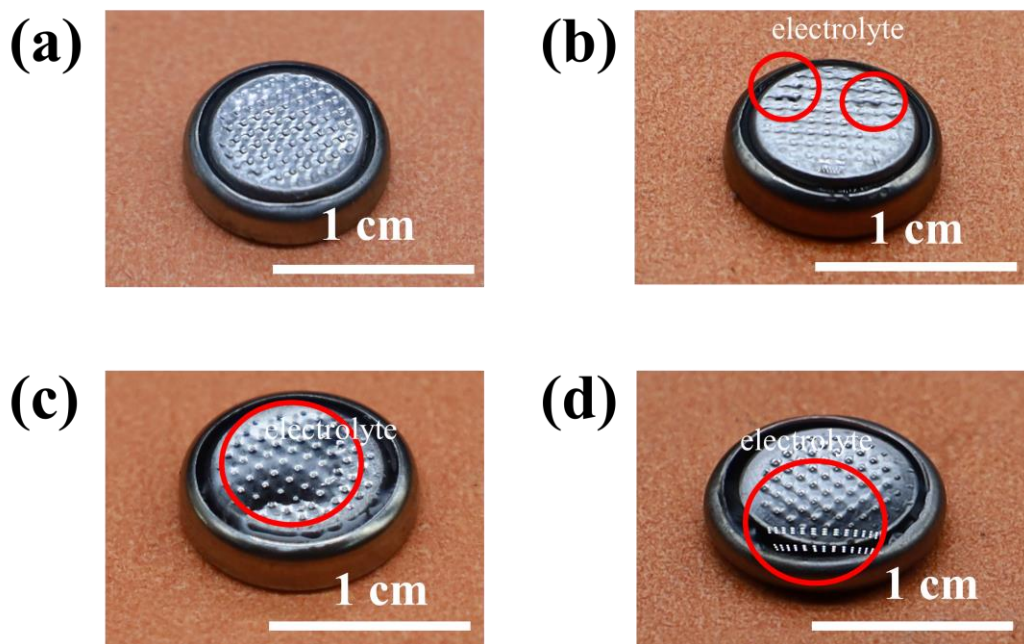


Figure S12. Leakage state of CR927 coin cell electrolyte at different strain values with mechanical compression testing. (a) 0 %, (b) 24.7 %, (c) 47.8 %, and (d) 60.3 %.

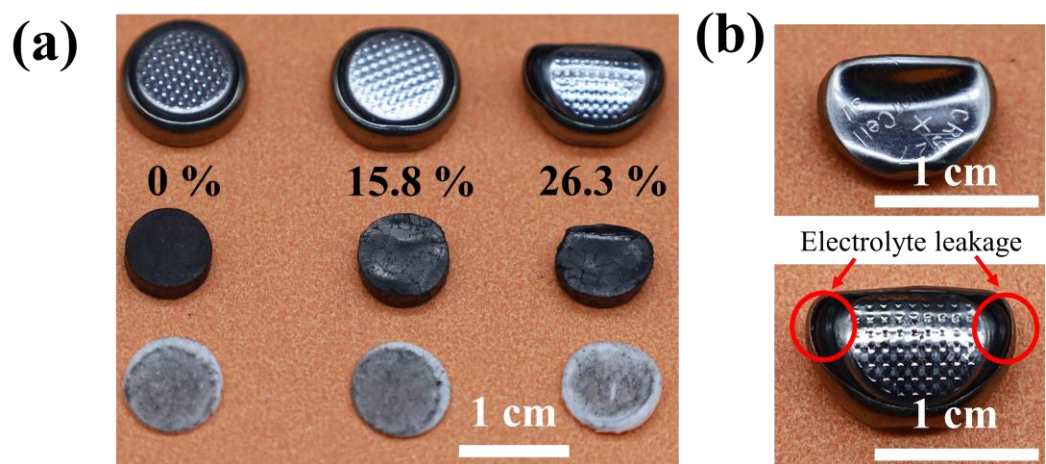


Figure S13. (a) and (b) are digital photographs of the coin cells after compression testing.



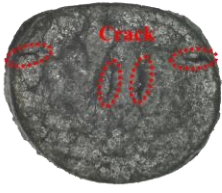
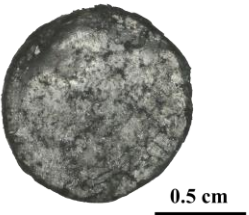


Strain value	0 %	15.8 %	26.3 %
Separator side			
Cathode shell side			

Figure S14. Photographs of the cathodes (90° placement) subjected to compression at constant speed of 1 mm/min with different strains.

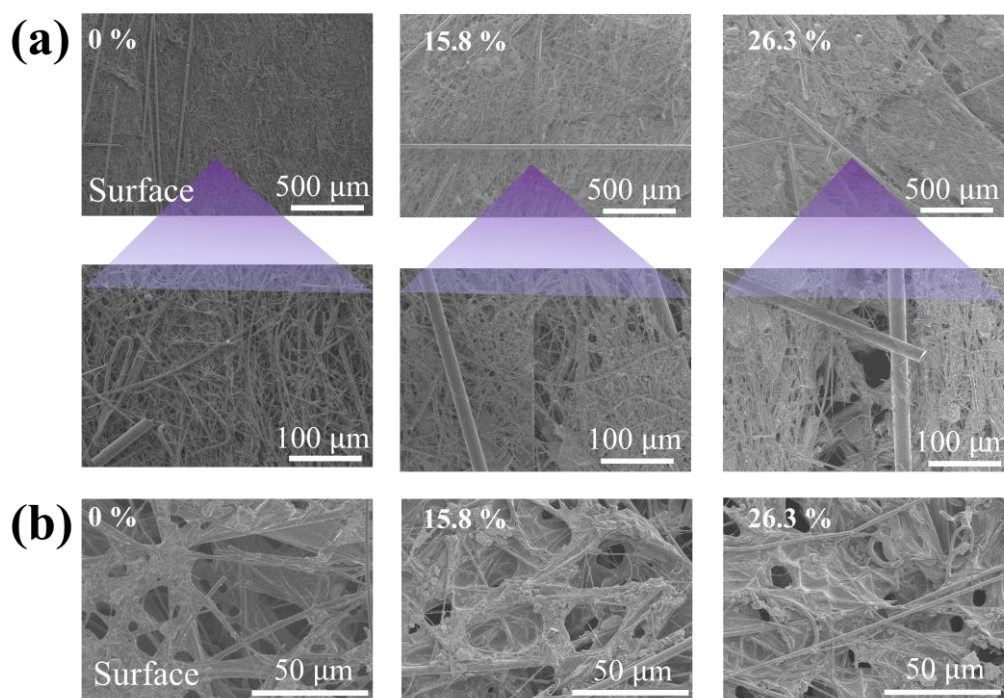


Figure S15. SEM images of separators (90° placement) subjected to compression at constant speed of 1 mm/min with different strains: (a) toward anode side and (b) toward cathode side.

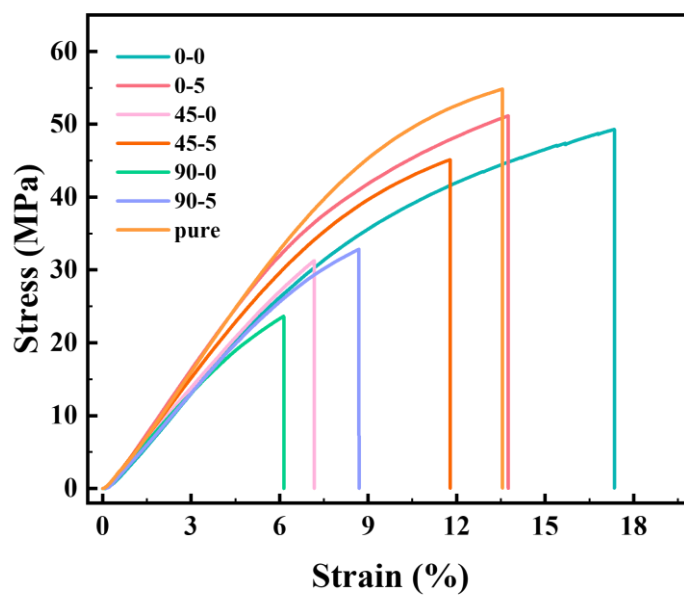


Figure S16. Three-point bending properties SPCs containing five CR927 coin cells at three placement conditions (0° , 45° , and 90°). The control samples was the polymer host with corresponding slots.

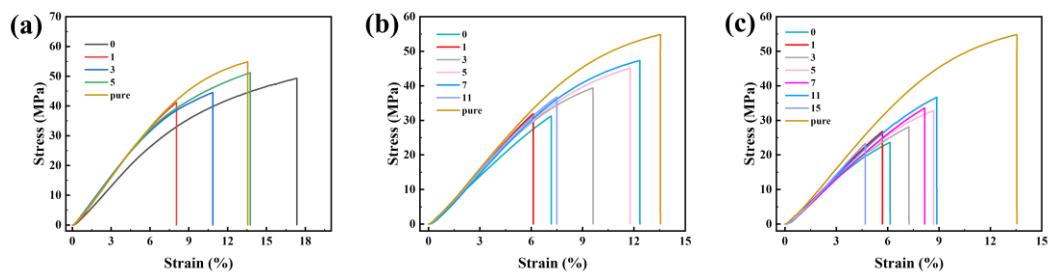


Figure S17. Three-point bending curves of SPCs with different placement condition of (a) 0° , (b) 45° , and (c) 90° .

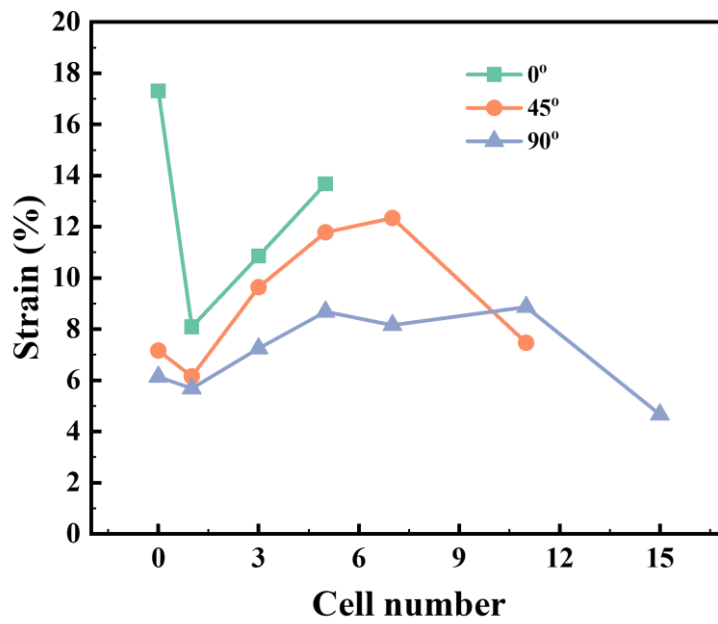


Figure S18. Summary showing the strain change during the three-point bending test of SPCs with different number of embedded cells.

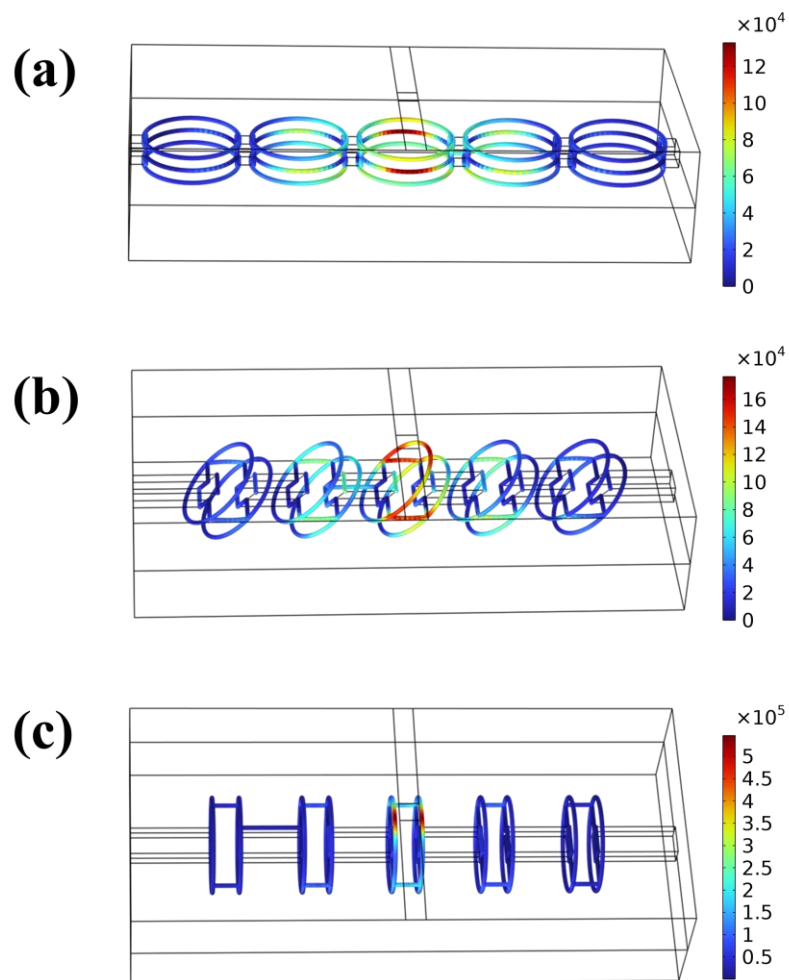


Figure S19. Simulated stress distribution of the plots in the polymer host under a constant pressure of 1 MPa with placement of (a) 0°, (b) 45°, and (c) 90°.

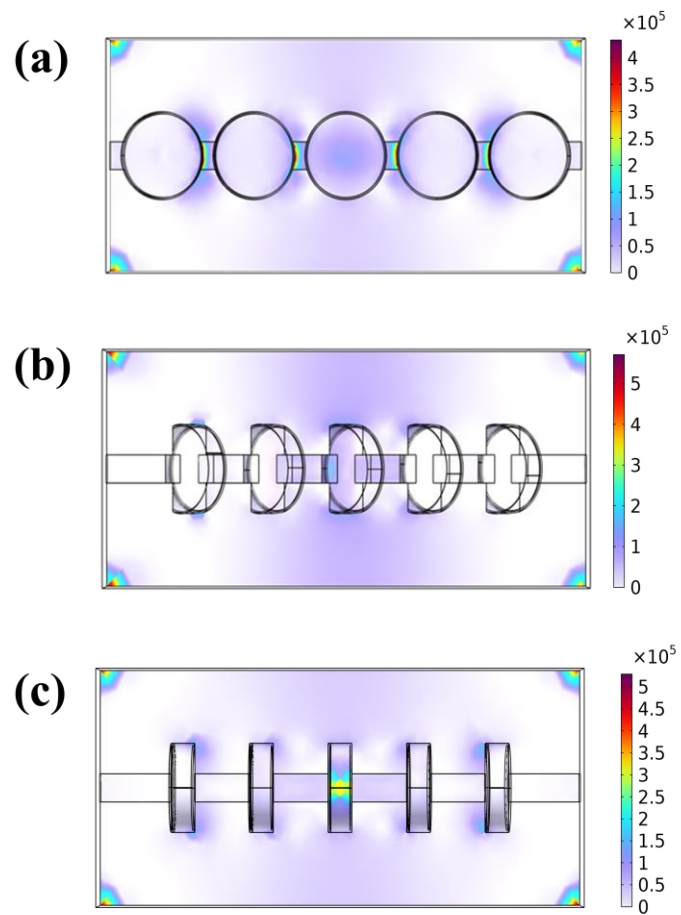


Figure S20. Simulated stress distribution of the polymer host under a constant pressure of 1 MPa with placement of (a) 0°, (b) 45°, and (c) 90°.

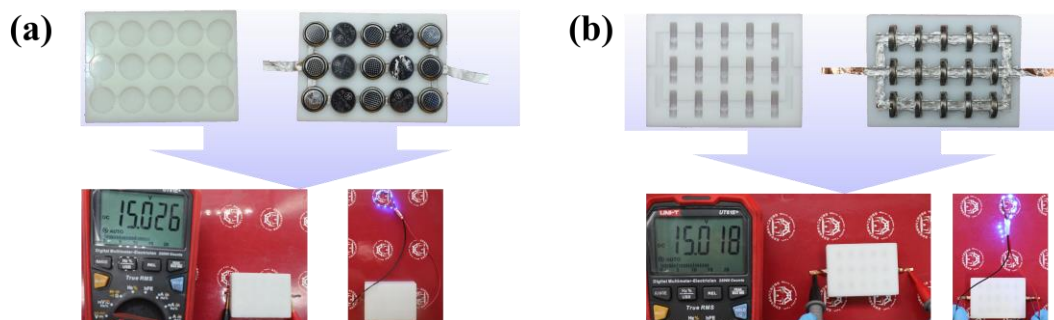


Figure S21. Photographs showing the assembly process and voltage of SPCs with different placement of coin cells in (a) 0° and (b) 90°.

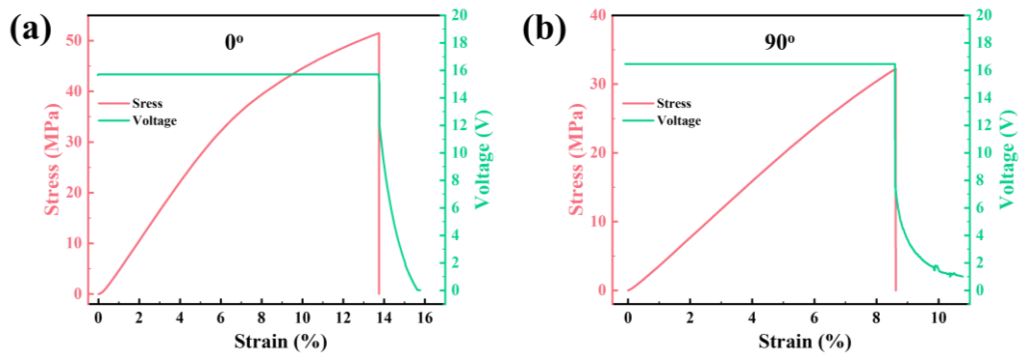


Figure S22. Voltage curves of SPCs with different placement condition of (a) 0° and (b) 90° .

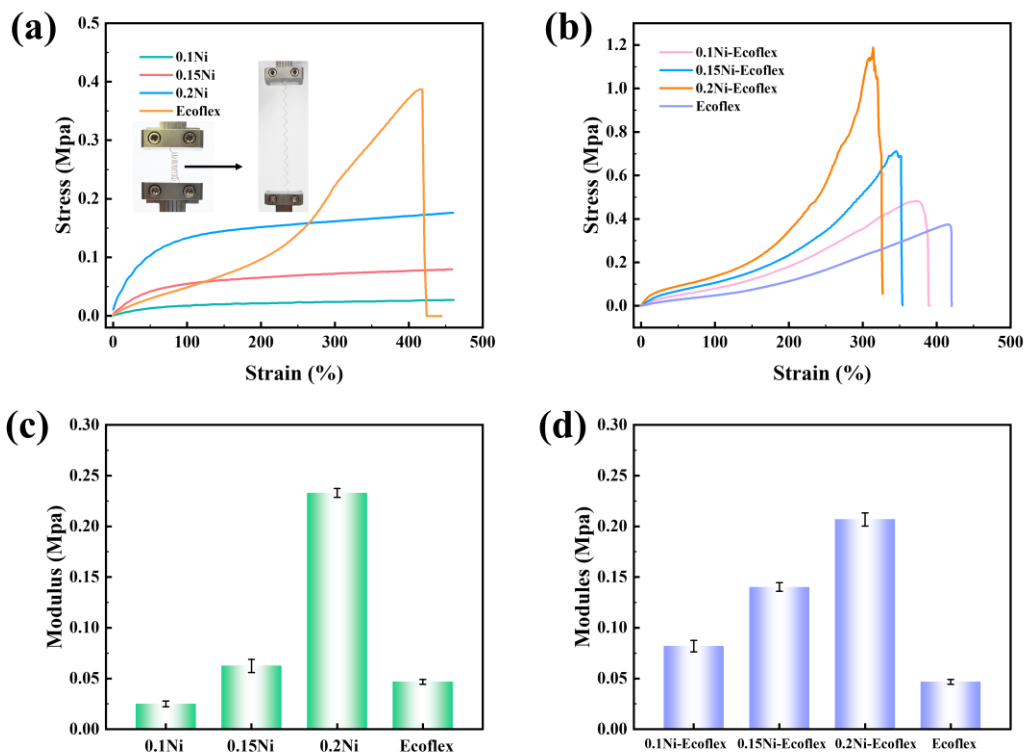


Figure S23. (a) and (b) are stress-strain curves of nickel metal wires, silicone rubber elastomer, and stretchable conductors. (c) and (d) are summary of elastic modulus of nickel metal wires, silicone rubber elastomer, and stretchable conductor materials. Note: The diameter of the nickel metal wire is 0.1 mm, 0.15 mm, and 0.2 mm.

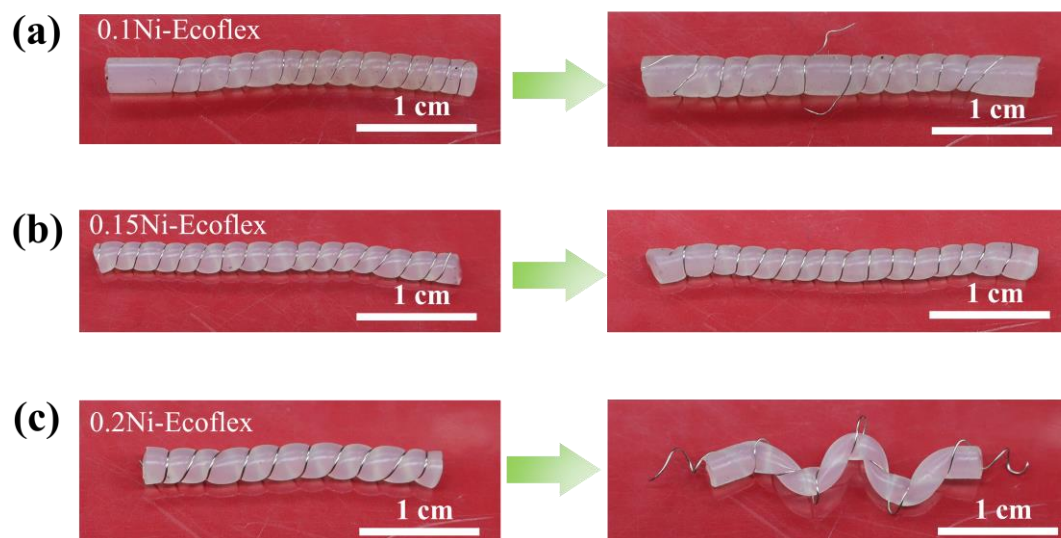


Figure S24. Photographs of stretchable conductors with different diameters of nickel metal wires after 50 stretching cycles: (a) 0.1 mm, (b) 0.15 mm, and (c) 0.2 mm.

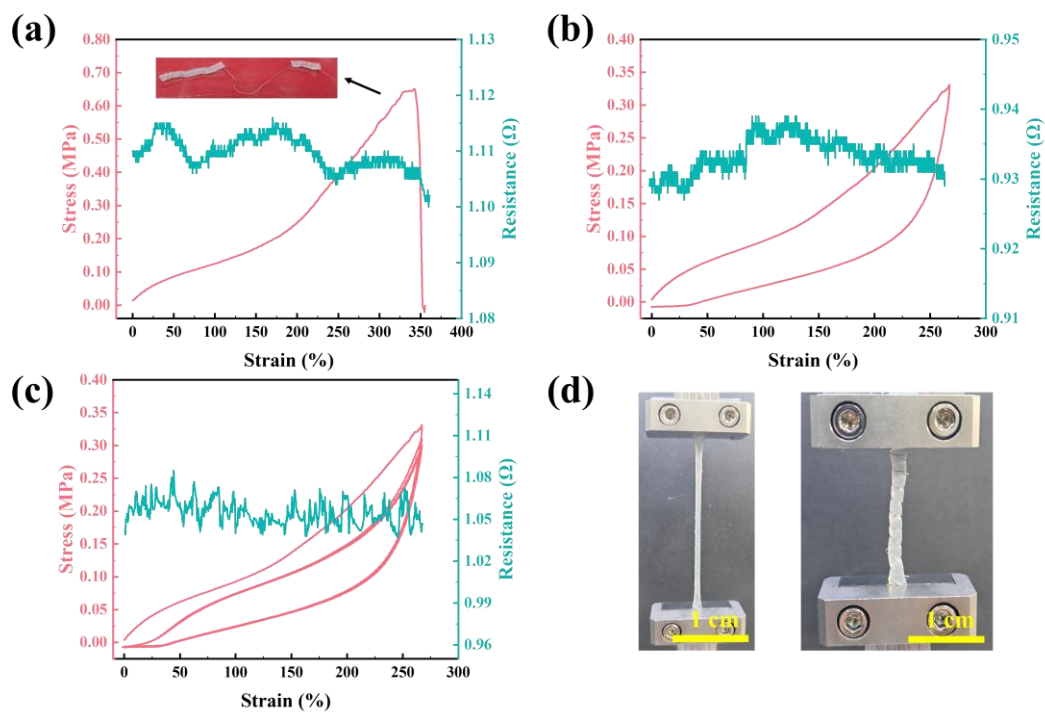


Figure S25. Resistance and stress variation of the stretchable conductor wrapped with 0.15-mm nickel metal wire on the 3 mm diameter silicone rubber elastomer: (a) ultimate stretching, (b) single-cycle stretching, and (c) multiple-cycle stretching. (d) Photograph of the stretchable conductor after cyclic stretching.

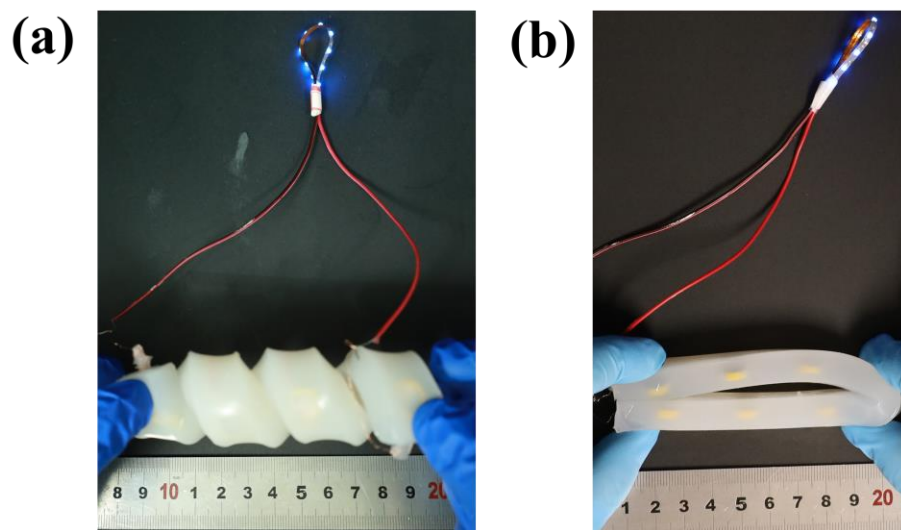


Figure S26. Flexibility demonstration of the SPC under (a) multiple twists and (b) bending state.

